# Relativistic Shear Flow between Electron–Ion and Electron–Positron Plasmas and Astrophysical Applications

Edison Liang[1], Wen Fu[1], and Markus Böttcher[2]
[1] Rice University, Houston, TX 77005, USA
[2] North-West University, Potchefstroom, 2520, South Africa
*Received 2016 November 27; revised 2017 July 20; accepted 2017 August 15; published 2017 September 25*

## Abstract

We present particle-in-cell simulation results of relativistic shear boundary layers between electron–ion and electron–positron plasmas and discuss their potential applications to astrophysics. Specifically, we find that in the case of a fast electron–positron spine surrounded by a slow-moving or stationary electron–ion sheath, lepton acceleration proceeds in a highly anisotropic manner due to electromagnetic fields created at the shear interface. While the highest-energy leptons still produce a beaming pattern (as seen in the quasi-stationary frame of the sheath) of order $1/\Gamma$, where $\Gamma$ is the bulk Lorentz factor of the spine, for lower-energy particles, the beaming is much less pronounced. This is in stark contrast to the case of pure electron–ion shear layers, in which anisotropic particle acceleration leads to significantly narrower beaming patterns than $1/\Gamma$ for the highest-energy particles. In either case, shear-layer acceleration is expected to produce strongly angle-dependent lepton (hence, emanating radiation) spectra, with a significantly harder spectrum in the forward direction than viewed from larger off-axis angles, much beyond the regular Doppler boosting effect from a co-moving isotropic lepton distribution. This may solve the problem of the need for high (and apparently arbitrarily chosen) minimum Lorentz factors of radiating electrons, often plaguing current blazar and GRB jet modeling efforts.

*Key words:* acceleration of particles – gamma-ray burst: general – gamma rays: general – radiation mechanisms: non-thermal – relativistic processes – quasars: general

## 1. Introduction

Recent large-scale particle-in-cell (PIC, Birdsall & Langdon 1991) simulations of relativistic collisionless shear boundary layers (SBLs) demonstrated efficient generation of large-scale transverse magnetic fields and particle energization from initially unmagnetized plasmas (Alves et al. 2012, 2014; Grismayer et al. 2013; Liang et al. 2013a, 2013b; Nishikawa et al. 2013, 2014, 2016). Relativistic SBLs are likely to arise from the interaction of relativistic outflows with slow-moving or stationary ambient medium, ranging from blazar jets (Ghisellini et al. 2005; Boettcher 2007) and gamma-ray bursts (GRB, Meszaros 2002; Piran 2004) to pulsar winds (e.g., Kargaltsev et al. 2015). Recent data modeling suggests that some blazar jets may have a spine-sheath structure (Ghisellini et al. 2005, 2010) that also solves certain problems of single-component jets (Maliani & Keppens 2009; Lyutikov & Lister 2010), and enhanced emission at the spine-sheath boundary may be the source of the observed limb brightening (Giroletti et al. 2004). Previous PIC simulations of SBLs focused on shear flows in which the plasma composition is the same on both sides of the shear boundary (e.g., pure electron–positron (e+e−) plasma (Liang et al. 2013a), pure electron–ion (e–ion) plasma (Alves et al. 2012; Grismayer et al. 2013; Nishikawa et al. 2013, 2014), or uniform mixtures of e+e− and e–ion plasma (Liang et al. 2013b). In this paper, we extend the previous works to include jumps in the plasma composition across the shear boundary. Specifically, we consider the case where the plasma is pure e+e− on one side of the SBL and pure e–ion on the other side. This case is most relevant to GRB jets and pulsar winds where the relativistic outflow from the central engine is conjectured to be e+e− plasma, while the ambient circumstellar matter (CSM) or insterstellar medium (ISM) is purely e–ion plasma, but it may also be applicable to

some blazars. We will first summarize the PIC simulation results in Section 2, and then discuss potential astrophysical applications in Section 3. As in our previous PIC simulations (Liang et al. 2013a, 2013b), we work in the frame in which the two opposing shear flows have equal Lorentz factors (Figure 1), which was previously called the center of momentum (CM) frame in the cases of homogenous composition. However, in the present case, as the two opposing flows have very different masses, this frame of equal Lorentz factors (ELF) is not the CM frame. All results presented below can be Lorentz boosted to the "laboratory" frame, where the ambient e–ion sheath is initially at rest, or to the "co-moving" frame of the outflow, where the e+e− spine is initially at rest.

First, we briefly summarize previous PIC simulations results on SBLs with homogenous composition. In the pure e+e− case (Liang et al. 2013a), transverse electromagnetic (EM) fields are first created by the oblique Weibel (Weibel 1959; Yang et al. 1993, 1994; Yoon 2007) and two-stream (Boyd & Sanderson 2003; Lapenta et al. 2007) instabilities caused by interface-crossing particle streams. These small-scale fields then grow into larger organized quasi-periodic magnetic flux ropes with alternating polarity. At late stage, they coalesce into large nonlinear eddy-like EM "vortices," extending up to hundreds of electron skin depths (Figure 2(f); Liang et al. 2013a). Particles are energized by $\boldsymbol{E} \times \boldsymbol{B}$ drift motions (Boyd & Sanderson 2003). Eventually, a steep power-law tail is formed that turns over at $\sim p_\circ/2$, where $p_\circ$ is the initial bulk Lorentz factor in the ELF frame. A key feature is the formation of a density trough at the SBL due to plasma expulsion by the self-created magnetic pressure. The EM energy saturates at $\sim 8\%$ of the total energy, which is dominated by the longitudinal P-mode at early times, but is dominated by the transverse T-mode at late times (Figure 2(c); Liang et al. 2013a).
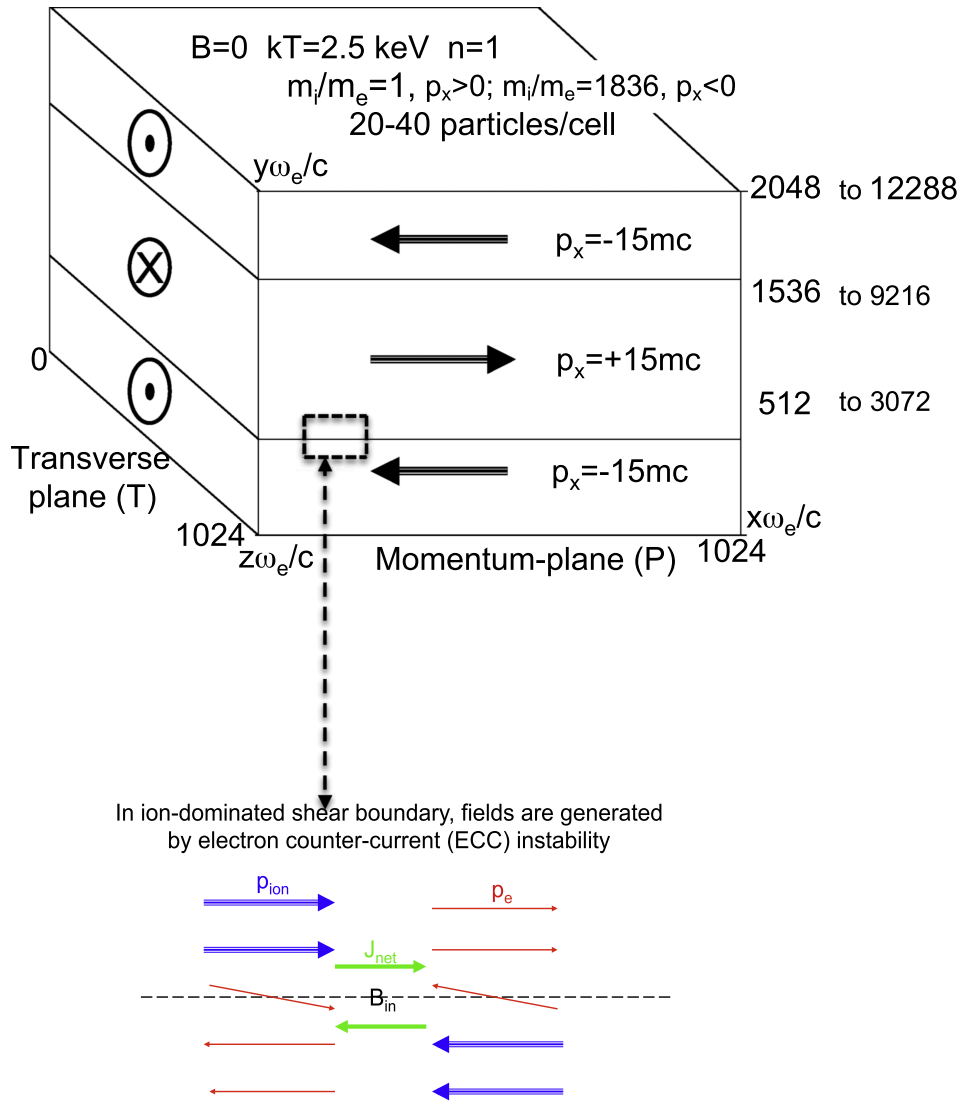
**Figure 1.** Setup of the (initially unmagnetized) shear flow PIC simulations of the e+e–ion sandwich. This paper focuses on the longitudinal P-mode evolution in the $x$–$y$ plane only, as the transverse T-mode saturates at very low level compared with the P-mode. In the present case, the plasma consists of right-moving e+e– pairs in the central 50% of the $y$-grid, referred to as the "spine," sandwiched between left-moving e–ion plasmas at the top 25% and bottom 25% of the $y$-grid, referred to as the "sheath." The simulation box has periodic boundary conditions on all sides. Inset: sketch illustrating d.c. magnetic field creation by the ECCI. Throughout this paper and in all figures, spatial scales are in units of the electron skin depth $c/\omega_e$.

In the pure e–ion ($m_i/m_e = 1836$) case (Alves et al. 2012, 2014, 2015; Grismayer et al. 2013), the development and structure of the SBL are completely different from the e+e– case. Due to their large mass difference, the ions are free-streaming, while the electrons are fluid-like (Gruzinov 2008; Grismayer et al. 2013). For cold electrons, the initial instability is a kinetic version of the Kelvin–Helmholtz instability (KHI, Chandrasekhar 1981; Zhang et al. 2009) involving only the electron fluid. Once the electrons achieve finite transverse momentum, either due to finite temperature or the Gruzinov instability, the electron counter-current instability (ECCI, Figure 1 inset; Alves et al. 2012; Liang et al. 2013b) dominates as electrons with finite transverse momentum cross over to the opposite flows, while the heavy ions do not. This leads to the formation of opposite current layers on the two sides the shear interface (Figure 1, lower panel), creating a monopolar slab of dc magnetic field (Figure 2(d), Alves et al. 2012; Liang et al. 2013b). The dc magnetic pressure expels the plasma, forming an effective ion vacuum gap at the interface (Liang

et al. 2013b). But the electrons, which have lower mass, are less evacuated than the ions. This leads to charge separation and formation of a triple layer (i.e., double capacitor), with strong $E_y$ fields pointing from both current layers toward the center of the SBL (Liang et al. 2013b). At the same time, $E_x$ fields (parallel to the current in the direction of the bulk motion) induced by $\partial B_z/\partial t$ are generated outside the current layers, which efficiently accelerate electrons to reach the ion energy. Eventually the electron distribution forms a narrow peak at $\sim p_o m_i c^2/2$. Unlike the pure e+e– case, there is no evidence of power-law tail formation. The EM energy saturates at $\sim12\%$ of the total energy and is completely dominated by the longitudinal P-mode. The transverse T-mode saturates at very low level, and contributes little to field creation or particle energization.

When we add e+e– plasmas uniformly to the e–ion shear flow, the results become more interesting. Besides the slab dc fields and ion vacuum gaps created at the interface by the ECCI, large-amplitude EM waves are created just outside the current layers, sandwiching the slab dc fields (Figure 2(e);
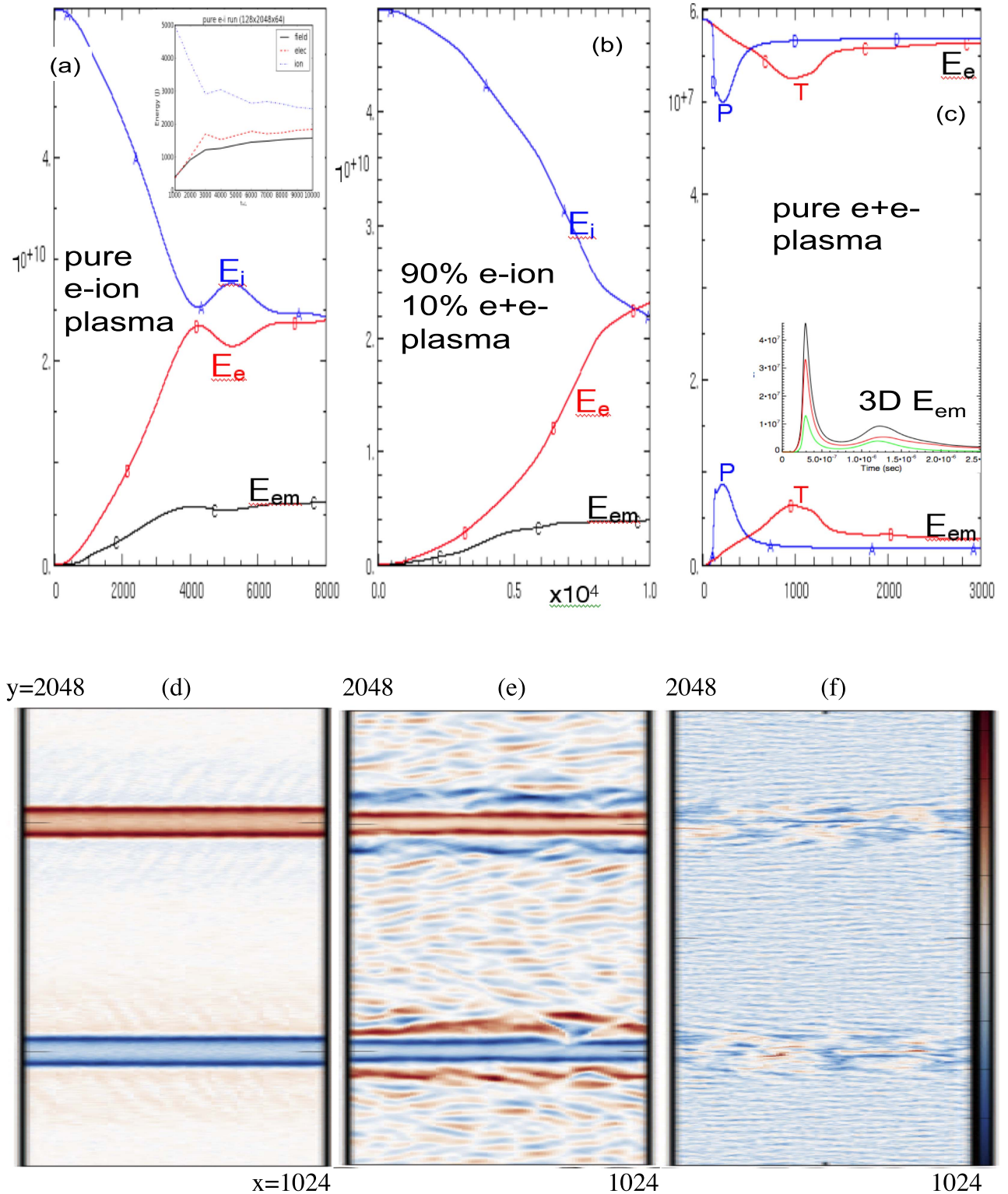
**Figure 2.** Top row: the evolution of energy components for three homogeneous SBL runs with $p_o = 15$: (a) pure e–ion plasma, (b) 90% e–ion + 10% e+e− plasma, and (c) pure e+e− plasma. Here, $E_{em}$ = EM field energy, $E_i$ = ion energy, and $E_e$ = lepton energy. For cases (a) and (b), only P-mode results are presented, as T-mode has negligible effect. Inset of (a) shows a 3D run compared with the 2D evolution. In case (c), we plot both P-mode and T-mode. In all cases, $E_{em}$ saturates at ~8%–12% of total energy, much higher than fields amplified by KHI (Zhang et al. 2009). In the two ion-dominated cases (a) and (b), the leptons reach energy equipartition with the ions after a finite time (figure from Liang et al. 2013a, 2013b). (bottom row) $B_z$ profiles of the same three runs at $t\omega_e = 3000$: (d) pure e–ion plasma, (e) 90% e–ion + 10% e+e− plasma, and (f) pure e+e− plasma. (Blue and red denote opposite polarities (figure from Liang et al. 2013a, 2013b).

Liang et al. 2013b). In addition to coherent acceleration by the dc fields toward the ion energy, leptons are also stochastically scattered by these EM waves to form a power-law tail, which at late times approaches a slope of ~−3 (Liang et al. 2013b). Hence, homogeneous e+e–ion shear flows may potentially explain the observed gamma-ray spectra of GRBs and blazars.
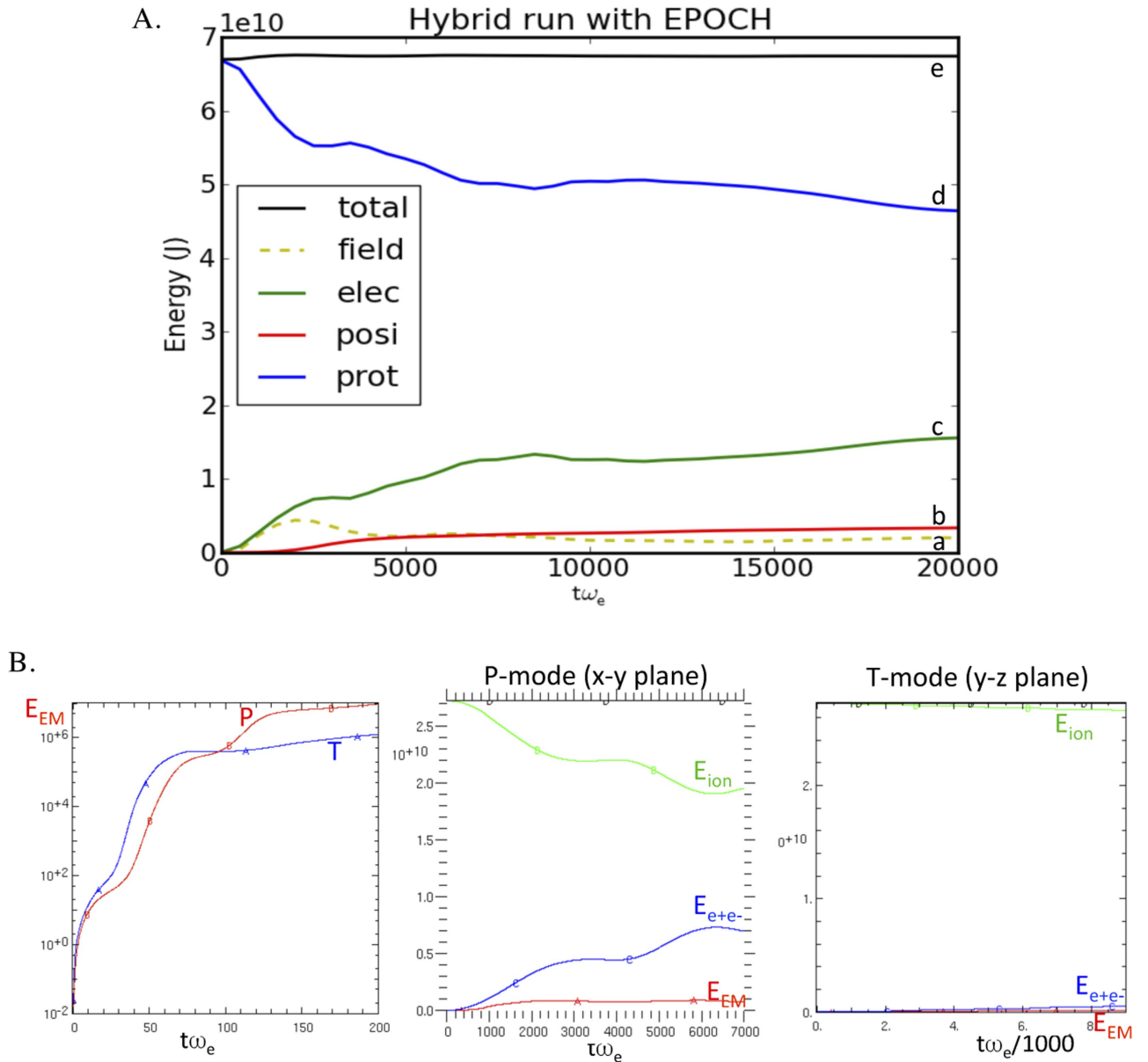
**Figure 3.** (A) Evolution of energy components of an EPOCH e+e–ion sandwich run in the x–y plane (P-mode): (a) EM field energy (brown dashed), (b) positron energy (red), (c) electron energy (green), (d) ion energy (blue), and (e) total energy (black). At late times, the electron energy saturates at ∼25% of total energy, the positron energy saturates at ∼4 % of total energy, and the EM field energy saturates at ∼3% of total energy. (B) Comparison of energy evolutions of Zohar-II e+e–ion sandwich run in the x–y plane (P-mode) with those in the y–z plane (T-mode). The left panel shows early exponential growth of $E_{EM}$ for both modes, with P-mode surpassing T-mode after $t\omega_e \sim 100$. The middle and right panels show the late-time saturation values using linear scales for all energies: $E_{ion}$ = ion energy (green), $E_{e+e-}$ = electron + positron energies (blue), $E_{EM}$ = electromagnetic energy (red). Comparing panel (A) with the middle panel of (B) shows that the two codes give similar results, even though Zohar-II energy conservation is much better than EPOCH.

Figure 2 summarizes the previous results of the three homogeneous shear flows discussed above (see Liang et al. 2013a, 2013b for details). A comment is in order here on the effect of the initial thickness of the velocity transition layer. While the steepness of the initial velocity gradient affects the linear growth rate of the ECCI, it does not affect the nonlinear saturation of the EM energy or the final structure of the SBL, as long as the initial velocity transition layer is thinner than the final thickness of the SBL (Figure 2).

## 2. PIC Simulations of e+e–ion Sandwich

In the current simulations, we used both the 2.5D (2D space, three-momenta) code Zohar-II (Langdon & Lasinski 1976; Birdsall & Langdon 1991) and the fully 3D code EPOCH

(Brady et al. 2012). In all ion-dominated shear flows, the T-mode in the y–z plane (Figure 1) saturates at low amplitude compared with the P-mode in the x–y plane, and has negligible effect also in this case (Liang et al. 2013b, confirmed by both 2.5D runs in the y–z plane and 3D runs). Hence, we focus on the 2D P-mode (Figure 1) results in the x–y plane (cf. discussions related to Figure 3 above), as we can use larger simulation boxes in 2D and run for longer times without any (artificial) interaction between the two SBLs (Figure 1). To compare with the previous results (Figure 2), in this section we present the results in the ELF frame for initial shear Lorentz factor $p_o = 15$ and initial temperature $kT_i = 2.5\,keV$ for electrons, positrons and ions ($m_+/m_e = 1$, $m_i/m_e = 1836$). In the ELF frame, the ions carry almost all of the initial energy.
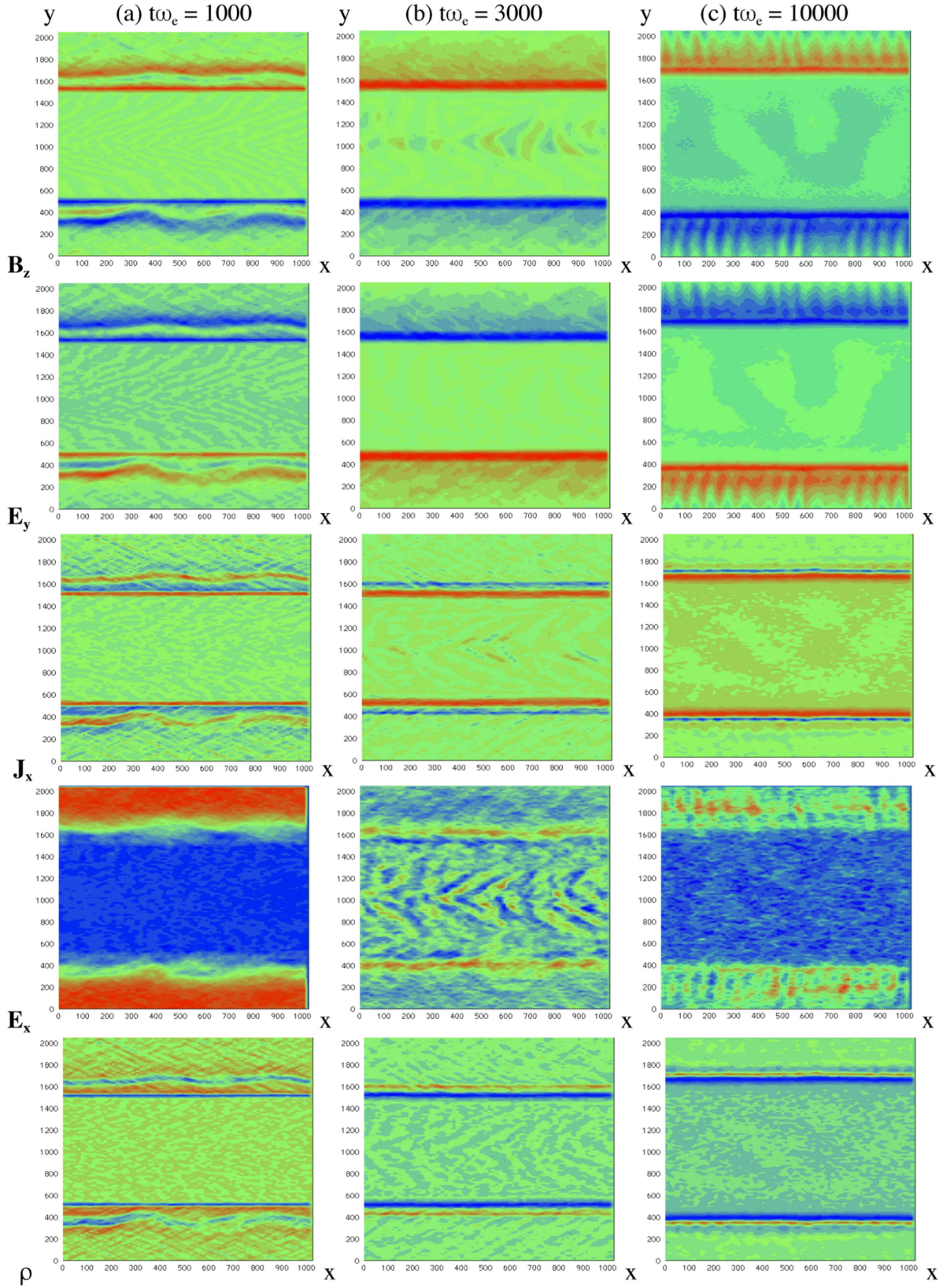
**Figure 4.** (a)–(c) From top to bottom: spatial profiles of $B_z$, $E_y$ $j_x$, $E_x$, $\rho$ = net charge = $(n_+ - n_-)$, for the e+e–ion sandwich SBL run at three different times: $t\omega_e$ = (a) 1000, (b) 3000, and (c) 10,000. The $B_z$ profiles at $t\omega_e$ = 3000 should be compared with the homogeneous SBL runs of Figures 2(d)–(f); (d) Fourier amplitude of $B_z(x, y = 300)$ at $t\omega_e$ = 10,000: $|B_z(k_x)|$ vs. $k_x$. The amplitude of NCI noise at $k_x \sim 300$ equals ~2% of the dc field amplitude; (e) 2D color contour maps of $B_z$ Fourier amplitude (left panels, linear scale), and power spectra (right figures, log scale to highlight the "spider leg" shapes of the NCI island mode) at two samples times. In panels (d) and (e), $k_x$ is in units of = $\pi/512\Delta x$, $k_y$ is in units of $\pi/1024\Delta y$. Bright yellow dots at (0, 0) denote the dc field whose amplitude is 30–200 times larger than the peak amplitude of the NCI island mode.
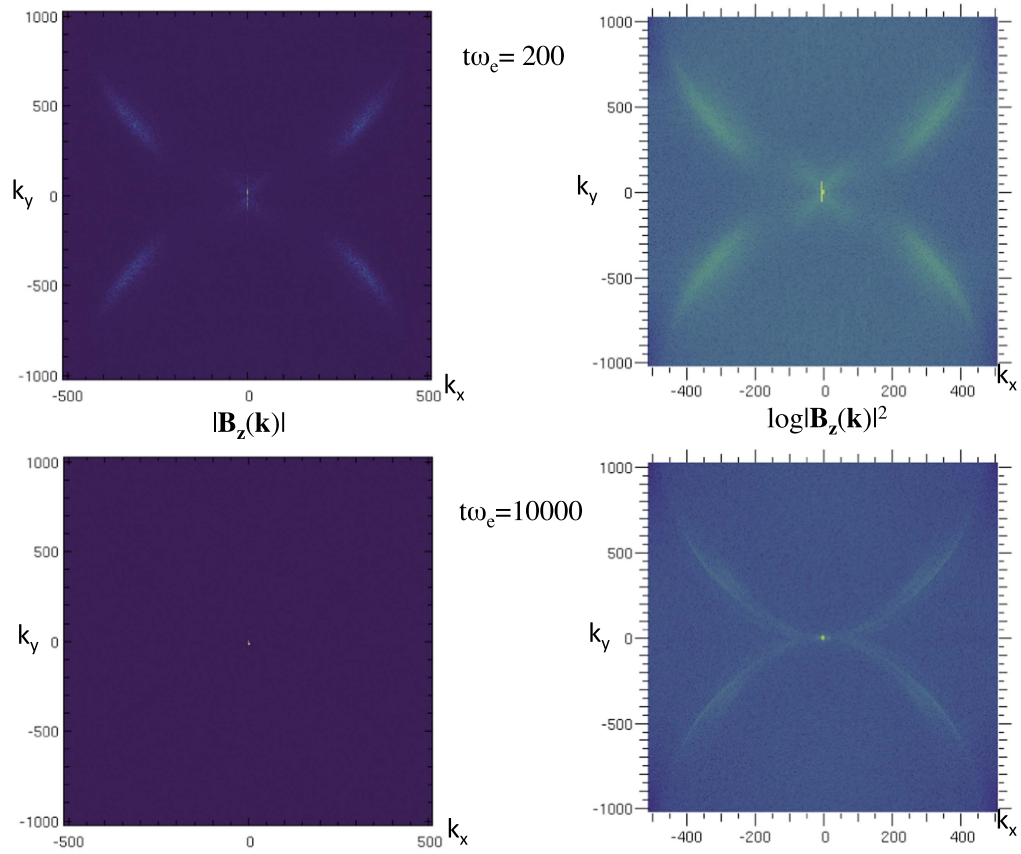
(d)          $|B_z(k_x)|(y=300)$



(e)



$t\omega_e = 200$

$|B_z(k)|$                    $\log|B_z(k)|^2$

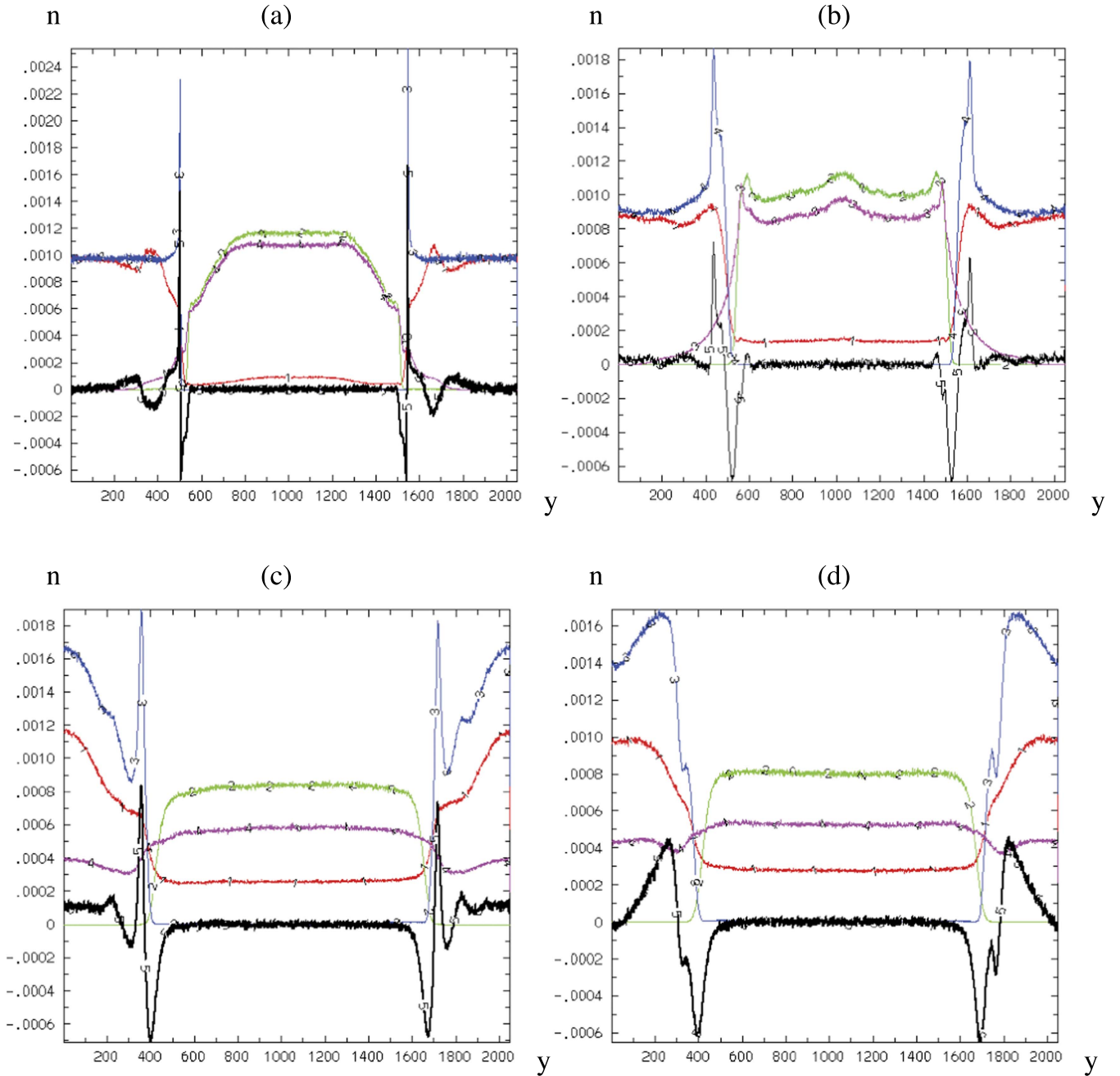$t\omega_e = 10000$
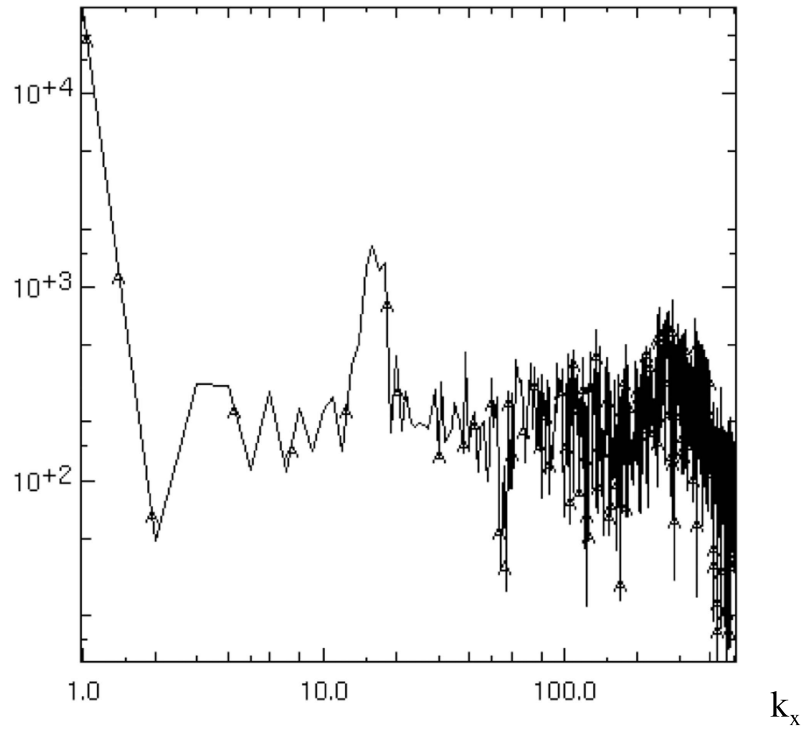
**Figure 4.** (Continued.)

**Figure 5.** Density profiles $n$ vs. $y$ (averaged over $x$), for the four particle species of the e+e–ion sandwich SBL run at four sample times: $t\omega_e =$ (a) 1000, (b) 3000, (c) 10,000, and (d) 16,000. Species: (1) red denotes initially left-moving electrons in e–ion sheath, (2) green denotes initially right-moving positrons in e+e− spine, (3) blue denotes initially left-moving ions in e–ion sheath, and (4) magenta denotes initially right-moving electrons in e+e− spine ((3) and (4) are switched in (b)). These density profiles highlight the net charge distribution (5) black as well as the diffusion of electrons into the opposing flows. At late times ($t\omega_e \geqslant 10,000$), the e+e− spine expands against and compresses the e–ion sheath.

Throughout this paper and in all of the figures, distances are measured in $c/\omega_e$ ($\omega_e$ = electron plasma frequency) and times are measured in $1/\omega_e$. We normalize the initial density $n = 1$ for all three species so that the cell size = electron skin depth. The plasmas are initially unmagnetized. Initially, right-moving e+e− plasma occupies the central 50% of the $y$-grid (hereafter called the "spine"), while left-moving e–ion plasma occupies the top 25% and bottom 25% of the $y$-grid (hereafter called the "sheath"). We call this configuration the e+e–ion sandwich (Figure 1). To study the effect of grid size, we varied the $y$-grid from 2048 cells up to 12,288 cells. The number of super particles per cell varied from 10 to 20 for each species. To

maximize numerical stability (see the discussions related to Figure 4(d)), we used time step $\Delta t = 0.1/\omega_e$ in all runs. For the $1028 \times 12,288$ EPOCH run, we ran to >400,000 time steps. Overall energy conservation was better than 1% for the Zohar-II code and was ∼5% for the EPOCH code. We found little difference between the main results of the two codes for the same setup.

Below, we first highlight the major results of the e+e–ion sandwich SBL in the ELF frame. Figure 3(A) shows the energy flow between ions, leptons, and EM fields for the P-mode from an EPOCH run. We see that the electron energy saturates at ∼25% of total energy, the positron energy saturates at ∼4%,

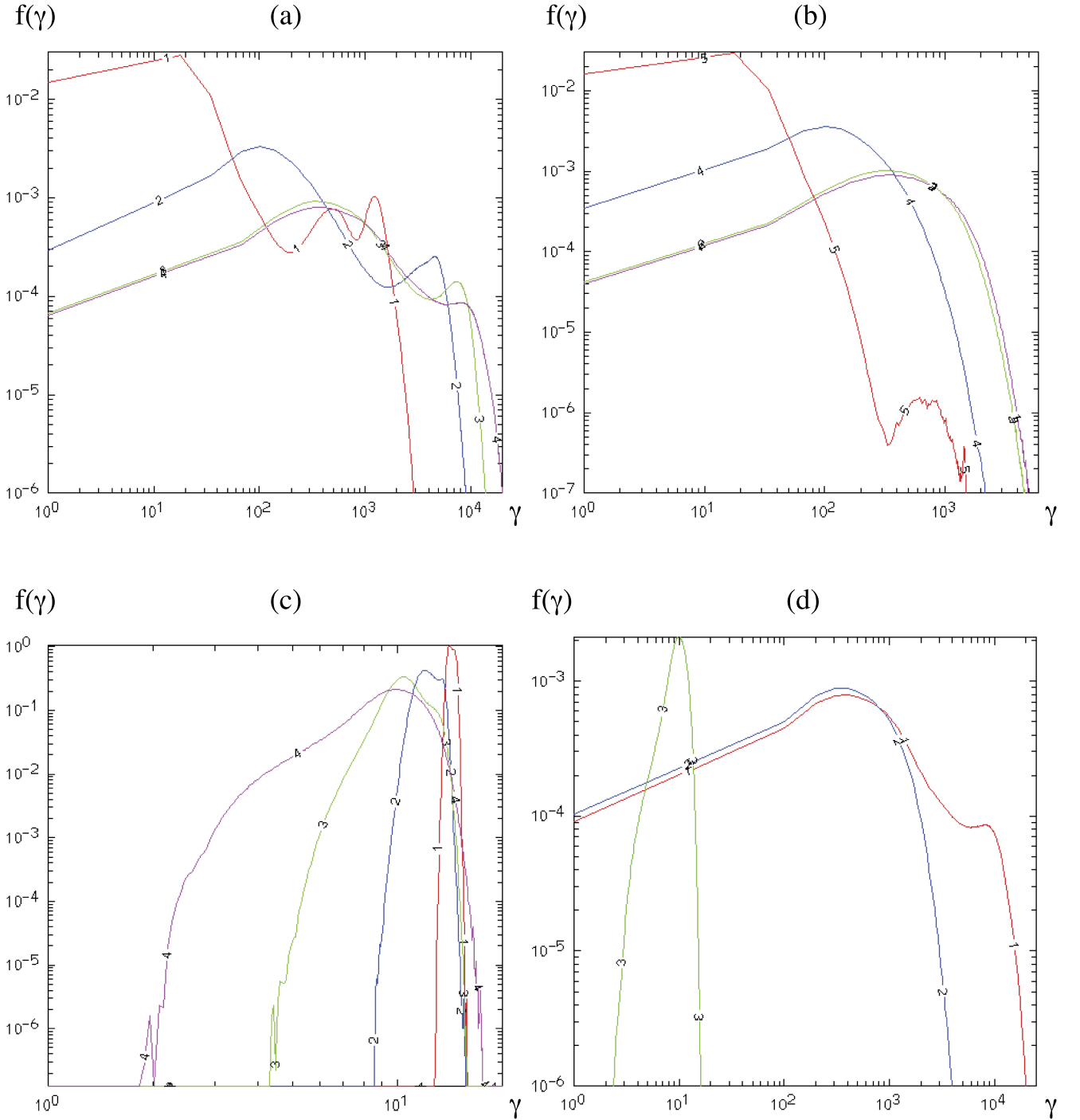**Figure 6.** (a) Evolution of the total electron distribution function $f(\gamma)$ (particle no. per unit $\gamma$) vs. $\gamma$ for the e+e–ion sandwich SBL shows that the electron spectrum continues to harden over time: $t\omega_e = 1000$ (red); 3000 (blue); 10,000 (green); 16,000 (magenta); (b) same as (a) for spine positrons showing that the positrons gain little energy after $t\omega_e \sim 10,000$; (c) same as (a) for sheath ions showing the deceleration of the ions over time; (d) comparison of electron (red), positron (blue), and ion (green) distributions at $t\omega_e = 16,000$. We see that the electrons have developed a hard power law between $\gamma_{min} \sim 400$ and $\gamma_{max} \sim 20,000$ with sharp cutoffs at both ends, plus a narrow peak at $\gamma \sim 10,000$.

and the EM energy saturates at $\sim 3\%$ of total energy, which is much lower than the homogeneous cases of Figure 2. Figure 3 (B) compares the energy evolution of the P-mode versus the T-mode from our Zohar-II run. The left panel shows the early exponential growth of electromagnetic energy $E_{EM}$ for the two modes. Despite a faster T-mode linear growth rate at early stages (Alves et al. 2015), P-mode surpasses T-mode after $t\omega_e \sim 100$. At late times, the P-model $E_{EM}$ is $\sim 30$ times larger than the T-mode $E_{EM}$ (middle and right panels). Moderate sized

3D runs (Figure 2(a) inset) also confirm that the P-mode dominates the T-mode. Thus, we are justified in focusing on the P-mode results in this paper. Figures 4(a)–(c) show the $B_z$ $E_y$, $J_x$, $E_x$ and net charge $\rho = (n_+ - n_-)$ profiles at $t\omega_e = 1000$, 3000 and 10,000, respectively. Comparing with Figures 2(d)–(f), we see that the e+e–ion sandwich SBL is a mix of the pure e–ion SBL and the pure e+e− SBL: the e–ion side of the SBL is dominated by strong persistent monopolar dc slab fields plus some long-wavelength (low-$k$) modes, while the e+e− side of
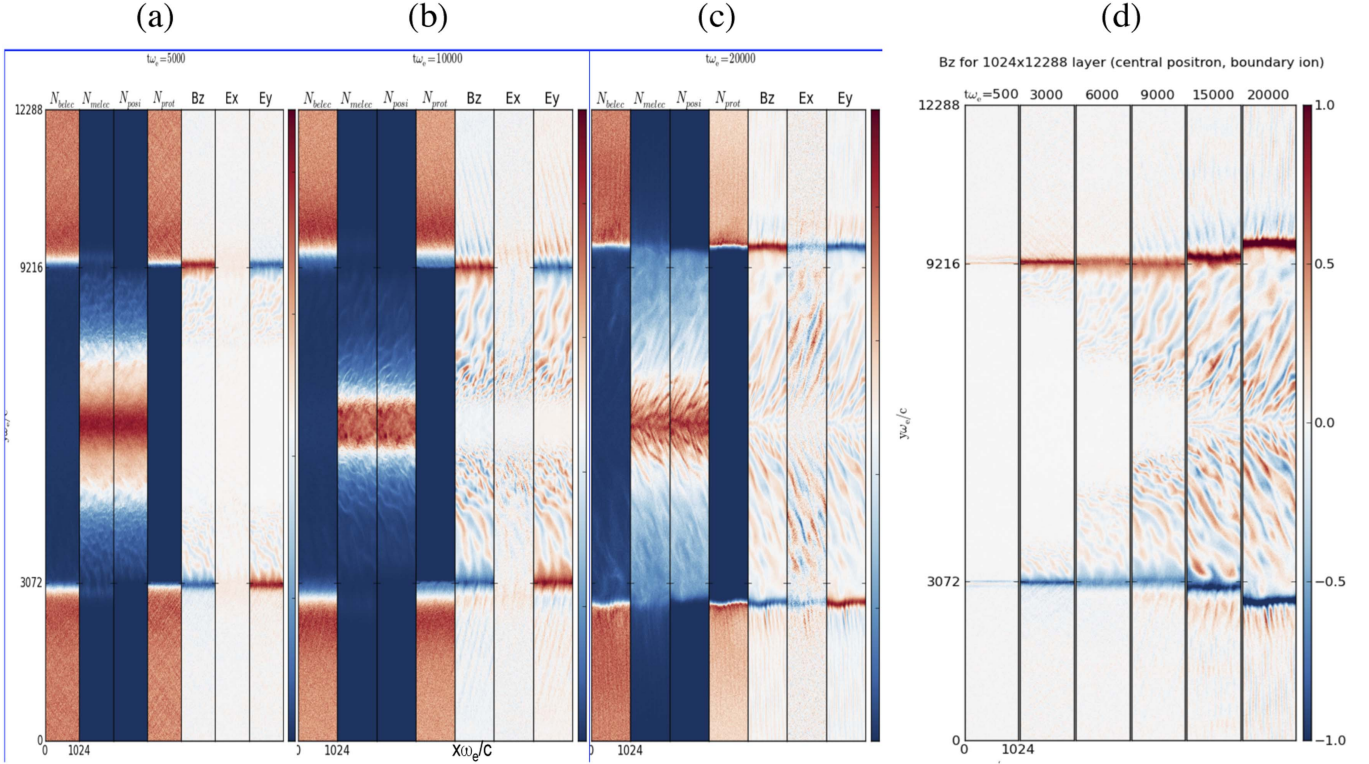
**Figure 7.** Time-lapse profiles of the e+e–ion sandwich run on a large (1024 × 12,288) grid using the EPOCH code (color bar has been renormalized between frames). Panels (a)–(c) show spatial profiles of the various physical variables at three sample times: $t\omega_e$ = (a) 3000, (b) 10,000, and (c) 20,000. (d) Evolution of the $\boldsymbol{B_z}$ field profile with time shows the expansion of the e+e− spine against the e–ion sheath at late times. The growth of EM waves in the spine is stronger than in Zohar-II (see Figure 4(c)). There is little interaction between the EM waves created by the two SBLs until $t\omega_e \sim 15{,}000$.

the SBL creates weaker bipolar ac fields. Global inductive $\boldsymbol{E_x}$ fields driven by $\partial B_z/\partial t$ permeate both sizes of the shear flow at early times (Figure 4(a), row 4). In the e–ion sheath, the $\boldsymbol{E_x}$ field points to the right, decelerating the protons while accelerating the electrons in the $-\boldsymbol{x}$ direction. In the e+e− spine, the $\boldsymbol{E_x}$ field points to the left, accelerating electrons in the $+\boldsymbol{x}$ direction and positrons in the $-\boldsymbol{x}$ direction.

An important issue in all PIC simulations with relativistic drifts is the effects of the numerical Cerenkov instability (NCI, Godfrey 1974, 1975; Birdsall & Langdon 1991; Yu et al. 2015). Zohar-II uses a variety of special numerical schemes to mitigate and suppress NCI, (e.g., Godfrey 1974, 1975; Godfrey & Langdon 1976; Godfrey & Vay 2013), and does many things differently from other finite difference PIC codes (B. Langdon 2017, private communication). As a result, the main NCI mode near the boundary of $k_x\Delta x/2\pi = 0.5$ is completely eliminated. The secondary NCI "island mode" near $k_x\Delta x/2\pi \sim 0.3$ (Li et al. 2016) is present in our shear flow runs, but its maximum amplitude is always kept below a few percent of the dc field amplitude. Figure 4(d) shows a sample Fourier spectrum of $B_z(x)$ at $y = 300$ of Figure 4(c). It shows that the NCI boundary mode at $k_x\Delta x/2\pi = 0.5$ is completely absent and that the island mode at $k_x\Delta x/2\pi \sim 0.3$ has a maximum amplitude equal to $\sim$2% of the dc field. Figure 4(e) shows the 2D color contour maps of $\boldsymbol{B_z}$ Fourier amplitudes (left-hand panels: linear scale) and power spectra (right-hand panels: log scale). The right-hand panels highlight the "spider leg" shapes of the island mode centered at $k_x\Delta x/2\pi \sim 0.3$. Integrating the power spectra over the four "spider legs," we find that the total energy of high-frequency noises (HFN) comes to 3%–6% of the dc field energy. Thus, the HFN has negligible effects on overall electron energization. We also studied the HFN amplitudes as a function of shear Lorentz

factor $p_\circ$ and time step $\Delta t$, and found that the maximum amplitude is always capped at a few percent of the dc fields, with no obvious dependence on $p_\circ$ or $\Delta t$. Hence NCI is well contained in the current runs and its undesirable effects on particle heating are small. Many groups are actively working on algorithms to completely eliminate or suppress NCI (e.g., Lehe et al. 2016; Li et al. 2016).

Figure 5 shows the evolution of the $x$-averaged densities of ion, electron, positron, and net charge as functions of $y$. This shows that an electron-dominated negative layer persists on the e+e− side of the SBL, while an ion-dominated positive layer persists on the e–ion side of the SBL, creating a double layer instead of the triple layer of the e–ion case (Figure 2). The currents associated with the charge separation sustain the dc slab field at the interface (Figure 4). Figure 6 shows the time evolution of the electron, ion, and positron energy spectra. At late times, the total electron spectrum consists of a quasi-power-law extending from $\gamma_{\min} \sim$ 400 to $\gamma_{\max} \sim 2 \times 10^4$ (=peak ion energy), plus a narrow peak around $\gamma \sim 10^4$. Detailed analysis suggests that the power-law electrons come from the e+e− spine, while the narrow peak population come from the e–ion sheath. The positron's spectrum is much softer than the electron's. Ions are continuously decelerated over time, peaking at $\gamma_i \sim 10$ at late times with a broad low-energy distribution (Figure 6(c)). In short, the e+e–ion sandwich SBL is capable of accelerating electrons to form a power-law tail extending to the ion peak energy ($\gamma_e \sim 20{,}000$ or 10 GeV in the ELF frame, Figure 6(d)). We carefully studied the particle energization in these shear flows and found that the electrodynamics is largely dominated by the dc field and low-$k$ modes, so that HFN, such as the NCI mode, has no net effect on the formation of the particle distributions in Figure 6.
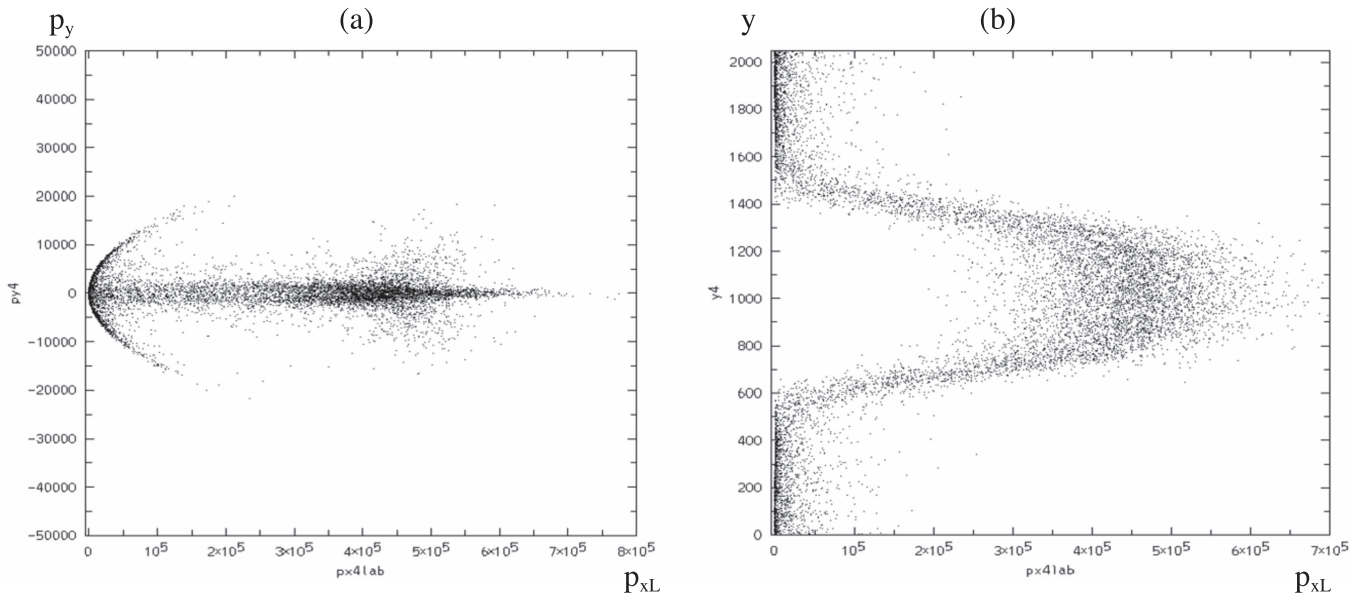
**Figure 8.** Phase plots of spine electrons for the pure e–ion run of Figure 2(a) at $t\omega_e = 10{,}000$, after Lorentz boosting $p_x$ to the "laboratory frame" in which the sheath is initially at rest: (a) $p_{xL}$ vs. $p_y$ and (b) $p_{xL}$ vs. $y\omega_e/c$. By this time, many of the spine electrons have diffused into the sheath located at $y\omega_e/c < 500$ and $y\omega_e/c > 1500$ of panel (b), and are decelerated and thermalized. These "cross over" electrons form the bow-shaped, low-energy population shown in panel (a), while the arrow-shaped high-energy population corresponds to electrons remaining in the spine ($500 < y\omega_e/c < 1500$ of panel (b)). Note the narrow beaming of the highest-energy electrons in panel (a), which are accelerated up to $\sim 0.5$ TeV. The broadening of the $p_y$ distribution around $p_x \sim 5 \times 10^5$ in panel (a) is caused by mid-plane collisions, which is likely an artifact of the small PIC box.

To study how the SBL results scale with box size, we have used the EPOCH code to perform larger box simulations. Figure 7 shows the SBL evolution for a $1024 \times 12{,}288$ EPOCH run. With the larger $y$-grid, EM fields originating from the two SBLs do not interact significantly until $t\omega_e \sim 15{,}000$. At late times, nonlinear oblique EM modes dominate the spine region and the e+e− spine expands against the e–ion sheath due to pressure imbalance. We believe that scattering by these nonlinear waves plays an important role in forming the late-time electron distribution. However, energy conservation in EPOCH runs (error $\sim 5\%$) is not as good as Zohar-II (error $<1\%$), and the EPOCH electron peaks tend to be broader than Zohar-II electron peaks. Both features hint that NCI and artificial electron heating may be more significant in EPOCH runs than in Zohar-II runs. Hence the EPOCH results of Figure 7 must be viewed with some caution, but they still serve to validate qualitatively the Zohar-II results based on smaller simulation boxes.

## 3. Applications to Grbs and Blazars

If GRB and blazar jets indeed have a spine-sheath structure, then our PIC simulations results above may be applicable to the local emission properties of the spine-sheath interface. To visualize the key differences in particle and radiation properties between a pure e–ion jet and a jet with e+e− spine surrounded by e–ion sheath, it is better to Lorentz boost the particle momenta from the ELF frame of Section 2 to the "laboratory" frame (LF) where the sheath is initially at rest, while the spine moves with bulk Lorentz factor $\Gamma = 451$. Figures 8 and 9 compare the phase plots for the two cases, after Lorentz boosting (in the $-x$ direction) from the ELF frame to the LF. We see that for the pure e–ion SBL (Figure 8), spine electrons are accelerated up to 0.5 TeV ($\sim$ decelerated ion energy in LF). Figure 8(a) shows that accelerated spine electrons reach extreme momentum anisotropy ($p_{xL} \gg p_y$), while their beam angle $|p_y/p_{xL}|$ decreases with increasing energy (Figure 10(a)).

On the other hand, for the e+e–ion sandwich SBL (Figure 9), the spine leptons are accelerated only up to $\sim 10$ GeV ($\sim$ accelerated ion energy in LF). While the accelerated spine lepton momenta are still anisotropic (Figure 9(a)), their beam angles are now much broader (Figure 10(b)). In fact, on average, they are broader than Doppler boosting of an isotropic distribution in the spine rest frame to the LF (red dashed line). Such big differences in lepton momentum distributions between the pure e–ion SBL and the e+e–ion sandwich SBL are easy to understand. In both cases, leptons are accelerated by EM fields created by the difference in lepton and ion masses. In the pure e–ion case, the spine ions move with initial $p_{xL} = +451 m_i c$ and carry all the initial energy. Their EM coupling to the spine electrons accelerates the electrons to the ion energy mainly via $E_x$ fields induced in the spine, which leads to $p_{xL} \gg p_y$ and extreme beaming (Figure 10(a)). On the other hand, in the e+e–ion sandwich case, the sheath ions are initially at rest and there is no ion in the fast-moving spine. EM fields created at the SBL eventually accelerate some sheath ions via energy transfer from the spine leptons, which move with initial $p_{xL} = +451 m_e c$ and carry all the initial energy. But the accelerated sheath ions can only reach low energy ($p_{xL} \sim$ few $m_i c$) due to their large mass, and the low ion energy limits the energy reachable by the leptons. At the same time, the $E_x$ fields induced in the spine are now much weaker, leading to broader lepton beaming (Figure 10(b)). Observationally, we therefore expect pure e–ion SBLs to emit much harder radiation with very narrow beaming and rapid time variability (due to variation of the observer view angle relative to the SBL orientation). In contrast, an e+e− spine interacting with an e–ion sheath should result in softer radiation, broader beaming and slower time variability. Such observational differences should be testable, especially for GRB jets where $\Gamma$ is large. Our PIC results also predict a stronger anticorrelation between lepton energy and beam angle for the pure e–ion SBL than for the e+e–ion sandwich SBL (Figure 10). We notice that while
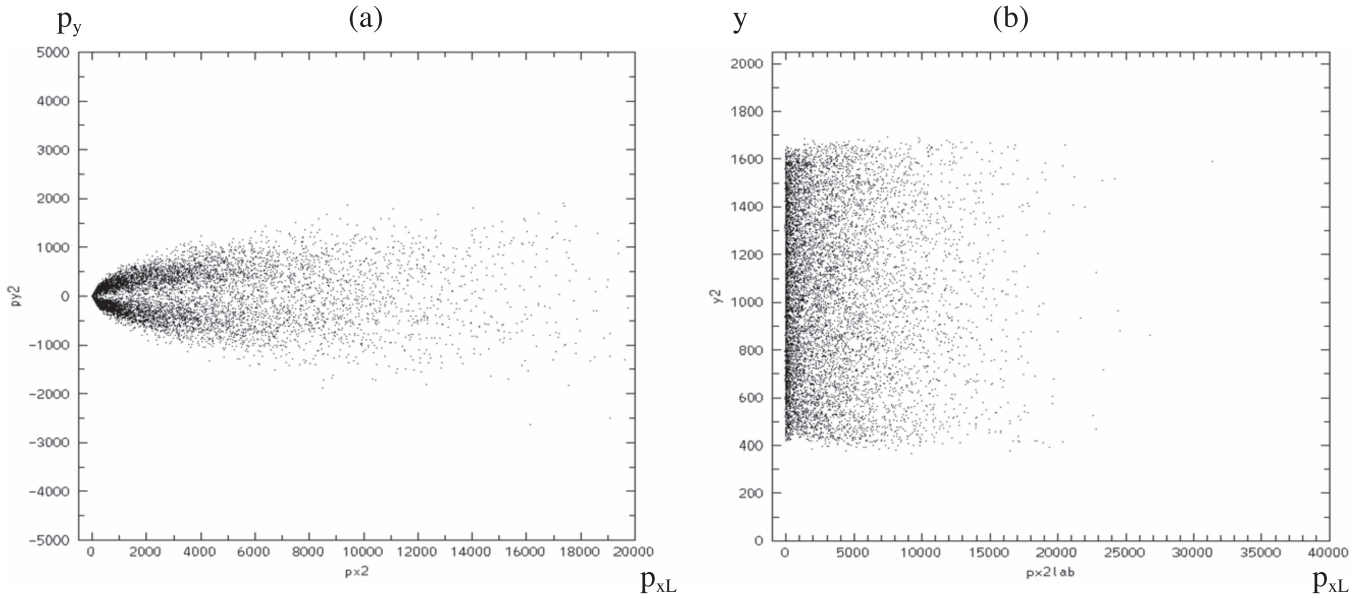
**Figure 9.** Phase plots of spine positrons for the e+e–ion sandwich SBL run at $t\omega_e = 10{,}000$, after Lorentz boosting $\boldsymbol{p_x}$ to the "laboratory frame" in which the sheath is initially at rest: (a) $\boldsymbol{p_{xL}}$ vs. $\boldsymbol{p_y}$ and (b) $\boldsymbol{p_{xL}}$ vs. $y\omega_e/c$. No spine positrons can diffuse into the sheath region. Compared with Figure 8, the "beaming" of the highest-energy positrons is much weaker, and they are only accelerated up to $\sim$10 GeV. Spine electron phase plots are similar.
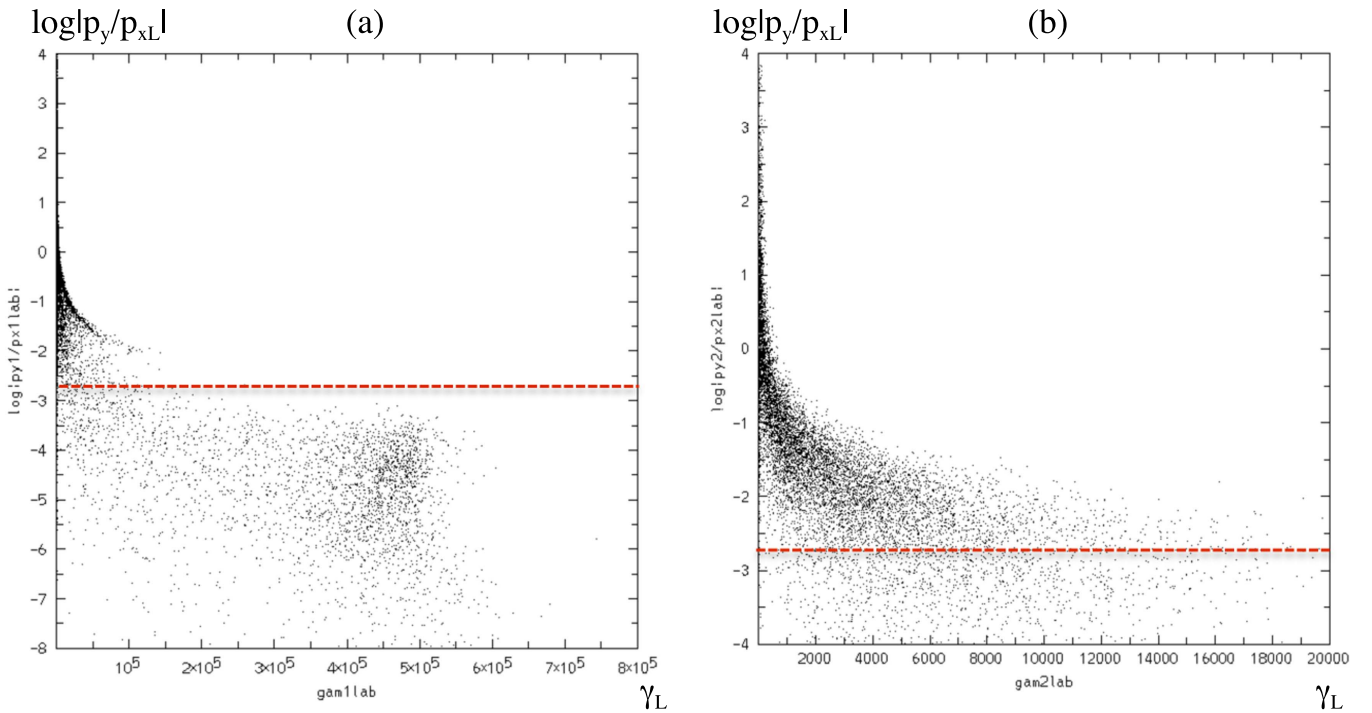


**Figure 10.** Distribution of the tangent of the "beam angle" ($=|p_y/p_{xL}|$) vs. Lorentz factor $\gamma_L$ in the "laboratory frame," at $t\omega_e = 10{,}000$: (a) for the spine electrons of the pure e–ion SBL and (b) for the spine positrons of the e+e–ion sandwich SBL. We see that in panel (a), most of the high-energy spine electrons (i.e., those that did not cross over to the sheath and get decelerated) have beam angles smaller than $1/\Gamma = 2.2 \times 10^{-3}$ (red dashed line). However, in panel (b), most of the spine positrons have beam angles larger than $1/\Gamma = 2.2 \times 10^{-3}$ (red dashed line). This means that the positron beam is broader than that from $\Gamma$ boosting of an isotropic lepton distribution in the spine rest frame.

some electrons diffuse into the opposing flows (Figure 8(b)), positrons (Figure 9(b)) and protons do not diffuse into the opposing flows, due to the magnetic field barrier. While the main results presented here are based on runs with $\Gamma = 451$ and are therefore more relevant to GRBs, we have performed other PIC simulations with $\Gamma = 10$'s that are more relevant to blazars. The results of those runs are qualitatively similar to

those presented here. Maximum particle energies and beam patterns both scale with the Lorentz factor as expected.

In summary, our PIC simulation results show that efficient lepton acceleration up to $\gamma_e \sim \Gamma_i m_i/m_e$ occurs in relativistic shear layers and proceeds in a strongly anisotropic manner. In the case of a fast electron–positron spine surrounded by a slow or stationary e–ion sheath, the spine-sheath interaction leads to

moderate acceleration of the sheath ions to $\Gamma \sim$ few, and a broadening of the angular distribution of spine leptons compared to a direct Doppler boosting of an isotropic lepton distribution in the co-moving frame of the spine. However, the highest-energy leptons with Lorentz factors of $\gamma_e >$ a few $10^3$ retain the typical $\sim 1/\Gamma$ beaming characteristic in the laboratory frame. This has important consequences for the observable radiation. Keeping in mind that in the process of Compton scattering by relativistic leptons, the scattered, high-energy photon emerges in the direction of the scattering lepton. Hence, if shear-layer acceleration in relativistic astrophysical jets is the dominant acceleration mechanisms of relativistic leptons, jets viewed in the forward direction will exhibit very hard radiation spectra, much beyond the usual spectral hardening effect due to bulk Doppler boosting of a co-moving isotropic particle distribution (which is just a shift of the peak frequency by factor $\Gamma$). On the other hand, jets viewed at substantial off-axis angles (assuming that the shear layer is largely parallel to the global jet axis) will be dominated by the radiation from the broadly beamed low-energy particles, and thus exhibit rather soft spectra.

We emphasize that this beaming effect becomes much more pronounced in the case of a pure e–ion shear layer. In the latter case, the highest-energy electrons are beamed into a very narrow cone, several orders of magnitude narrower than the $\sim 1/\Gamma$ beaming characteristic of bulk Doppler boosting, while lower-energy particles still exhibit significant beaming. The narrow beaming may also explain the minute-scale rapid time variability of some blazars (F. Tavecchio & G. Ghisellini 2017, private communication).

The strong energy dependence of the angular distribution of the relativistic leptons for spine-sheath jets has important consequences for the high-energy emission from relativistic jet sources, such as blazars and GRB. Essentially all current works on modeling the spectral energy distributions of blazars based on leptonic radiation scenarios assume a relativistic electron distribution which is isotropic in the co-moving frame of the bulk motion of the jet. In such models, very often quite high minimum Lorentz factors of the relativistic electron distribution have to be assumed (e.g., Ghisellini et al. 2010; Boettcher et al. 2013), which often appear to be rather arbitrarily chosen. Yet our PIC results naturally predict such low-energy cutoffs (Figure 6(d)). Such a low-energy cutoff is necessary to reproduce the observed hard X-ray—gamma-ray spectra of blazars. This is particularly relevant for the spine-sheath model of Ghisellini et al. (2005) and Tavecchio & Ghsiellini (2008). In this model, the radiative interaction between the spine and the sheath is proposed to increase the radiative efficiency due to relative Doppler boosting of the radiation fields produced in the two jet components. In this scenario, obviously, the shear-layer acceleration mechanisms investigated here becomes relevant. However, Ghisellini et al. (2005) and Tavecchio & Ghsiellini (2008) assumed isotropic electron distributions in the respective co-moving frames, and also required large minimum electron Lorentz factors, at least in the spine. The differential beaming of leptons in the laboratory frame resulting from our PIC simulations provides a natural explanation for such hard spectra for blazars, in which we view the jet at a small angle from the jet axis. A detailed investigation of the resulting radiation characteristics based on PIC data (Hededal & Norlund 2005; Sironi & Spitkovsky 2009) is beyond the scope of the current paper and will be studied in follow-up works.

A problem similar to the low minimum electron Lorentz factors in blazars discussed above exists also for GRBs: The prompt hard X-ray/soft gamma-ray spectra of many GRBs show very hard low-energy slopes, even harder than a self-absorbed synchrotron spectrum (Rybicki & Lightman 1979), which have been considered as an argument against a synchrotron origin of the high-energy emission of GRBs (the "line of death" problem, Preece et al. 1998). This in turn stimulated a discussion on possible "photospheric" (optically thick) emission components in GRB spectra (e.g., Ryde 2005; Ryde et al. 2006). The extreme angle dependence of the lepton spectra found in our studies may also provide a solution for such unexpectedly hard X-ray—gamma-ray spectra.

The two cases of electron–positron versus e–ion spine compositions differ markedly in the beaming characteristics of high-energy leptons. In the case of an electron–positron spine, even the highest-energy leptons will not exhibit a beaming pattern narrower than $\sim 1/\Gamma$, and substantial high-energy emission is still expected to be observable under moderate viewing angles characteristic of radio galaxies. In the case of GRB jets, this scenario predicts a substantial chance of detecting gamma-ray emission from GRBs at off-axis angles $\theta_{obs} > 1/\Gamma$. On the contrary, if the jet composition is pure e–ion plasma in both the spine and the sheath, one expects a small population of sources viewed under very small viewing angles with $\theta_{obs} \ll 1/\Gamma$, with very hard gamma-ray spectra (such as those detected by LAT onboard Fermi Observatory), while a much larger population of off-axis sources with $\theta_{obs} > 1/\Gamma$ appear to have softer spectra. The recently emerging class of extreme BL Lac objects (e.g., Bonnoli et al. 2015) may possibly represent the small population of extremely narrowly beamed, very-hard-spectrum blazars expected in the e–ion shear acceleration scenario.

### ORCID iDs

Wen Fu https://orcid.org/0000-0003-2646-0577
Markus Böttcher https://orcid.org/0000-0002-8434-5692

### References

Alves, E. P., Griesmayer, T., Fonseca, R. A., & Silva, L. O. 2014, NJPh, 16, 035007
Alves, E. P., Griesmayer, T., Fonseca, R. A., & Silva, L. O. 2015, PhRvE, 92, 021101
Alves, E. P., Grismayer, T., Martins, S. F., et al. 2012, ApJL, 746, L14
Birdsall, C., & Langdon, A. B. 1991, Plasma Physics via Computer Simulation (Bristol: IOP)
Boettcher, M. 2007, Ap&SS, 309, 95
Boettcher, M., Reimer, A., Sweeney, K., & Prakash, A. 2013, ApJ, 768, 54

Bonnoli, G., Tavecchio, F., Ghisellini, G., & Sbarrato, T. 2015, MNRAS, 451, 611
Boyd, T., & Sanderson, J. 2003, Physics of Plasmas (Cambridge: Cambridge Univ. Press)
Brady, C., Bennett, K., Schimtz, H., & Ridgers, C. 2012, EPOCH Users Manual v4.3.4 (Coventry, UK: Univ. Warwick Centre for Fusion, Space and Astrophysics)
Chandrasekhar, S. 1981, Hydrodynamic and Hydromagnetic Stability (New York: Dover)
Ghisellini, G., Tavecchio, F., & Chiaberge, M. 2005, A&A, 432, 401
Ghisellini, G., Tavecchio, F., Foschini, L., et al. 2010, MNRAS, 402, 497
Giroletti, M., Giovannini, G., Feretti, L., Cotton, W. D., & Edwards, P. G. 2004, ApJ, 600, 127
Godfrey, B. 1974, JCoPh, 15, 504
Godfrey, B. 1975, JCoPh, 19, 58
Godfrey, B., & Langdon, B. 1976, JCoPh, 20, 251
Godfrey, B., & Vay, J. 2013, JCoPh, 248, 33
Godfrey, B., & Vay, J. 2014, JCoPh, 261, 1
Grismayer, T., Alves, E. P., Fonseca, R. A., & Silva, L. O. 2013, PhRvL, 111, 015005
Gruzinov, A. 2008, arXiv:0803.1182
Hededal, C., & Norlund, A. 2005, arXiv:astroph0511662
Kargaltsev, O., Cerutti, B., Lyubarsky, Yu., & Striani, E. 2015, SSRv, 191, 391
Langdon, A. B., & Lasinski, B. 1976, in Meth. Comp. Phys. 16, ed. B. Alder et al. (New York: Academic), 327
Lapenta, G., Markidis, S., Marocchino, A., et al. 2007, ApJ, 666, 949
Lehe, R., Kirchen, M., Godfrey, B., et al. 2016, PhRvE, 94, 053305
Li, F., Yu, P., Xu, X., et al. 2016, CoPhC, submitted, arXiv:1605.01496v1
Liang, E., Boettcher, M., & Smith, I. 2013a, ApJL, 766, L19
Liang, E., Fu, W., Boettcher, M., Smith, I., & Roustazadeh, P. 2013b, ApJL, 779, L27
Lyutikov, M., & Lister, M. 2010, ApJ, 722, 197
Maliani, Z., & Keppens, R. 2009, ApJ, 705, 1594
Meszaros, P. 2002, ARA&A, 40, 137
Nishikawa, K., Frederiksen, J., Nordlund, A., et al. 2016, ApJ, 820, 94
Nishikawa, K., Hardee, P., Dutan, I., et al. 2014, ApJ, 793, 60
Nishikawa, K., Hardee, P., Zhang, B., et al. 2013, AnGeo, 31, 1535
Piran, T. 2004, RvMP, 76, 1143
Preece, R. D., Briggs, M. S., Mallozzi, R. S., et al. 1998, ApJL, 506, L23
Rybicki, G., & Lightman, A. 1979, Radiative Processes in Astrophysics (San Francisco, CA: Freeman)
Ryde, F. 2005, ApJL, 625, L95
Ryde, F., Björnsson, C.-I., Kaneko, Y., et al. 2006, ApJ, 652, 1400
Sironi, L., & Spitkovsky, A. 2009, ApJL, 707, L92
Tavecchio, F., & Ghsiellini, G. 2008, MNRAS, 385, L98
Weibel, S. 1959, PhRvL, 2, 83
Yang, T., Arons, J., & Langdon, B. 1994, PhPl, 1, 3059
Yang, T., Gallant, Y., Arons, J., et al. 1993, PhFlB, 5, 3369
Yoon, P. 2007, PhPl, 14, 024504
Yu, P., Xu, X., Decyk, V., et al. 2015, CoPhC, 192, 32
Zhang, W., MacFadyen, A., & Wang, P. 2009, ApJL, 692, L40